Control and Design of a Novel Dual Multiplexing Soft Open Point With Small Volume

Yutong Chen, Wu Chen, *Senior Member, IEEE*, Haixi Zhao, Zewei Hao, Jianxi Lan, *Member, IEEE*, Xuze Wang, Xin Li, Runyan Sha, Jiangfeng Wang, *Member, IEEE*, Xin Li, *Member, IEEE*, Wei Jiang, *Senior Member, IEEE*, and Yubo Yuan, *Member, IEEE*

***Abstract*—The soft open point (SOP) technology enables flexible power regulation in distribution networks, making it a critical tool for grid modernization. However, existing SOP topologies face challenges such as the need for numerous submodules and low efficiency. This article addresses the flexible interconnection of 10 kV medium-voltage distribution networks by proposing a compact topology called dual multiplexing SOP (DM-SOP), based on high-voltage SiC MOSFETs. The DM-SOP topology exhibits modular characteristics and enables decoupled power control between two feeders. It offers advantages over traditional SOP topologies, including a reduced footprint, fewer switches, and high efficiency. This article presents the novel DM-SOP topology, its operational principles, control strategies, and operational ranges. Finally, through feeder interconnection simulations and the construction of a 1.5 kW low-power prototype for experimental validation, the feasibility of the DM-SOP topology, as well as the effectiveness of the control and energy balancing strategies, are confirmed.**

***Index Terms*—Distribution network (DN), multiplexing module, medium voltage converter, soft open point.**

NOMENCLATURE

BTB-MMC	Back-to-back modular multilevel converter.
BTB-NPC	Back-to-back neutral point clamped.
BTB-VSC	Back-to-back voltage source converter.
CHB	Cascaded H-bridge.
DM-SOP	Dual multiplexing soft open point.
IM	Interconnect module.
MM	Multiplexing module.
SiC	Silicon carbide.
SOP	Soft Open Point.
THD	Total harmonic distortion.
x	Instantaneous value.
X	Amplitude value.
$\vec{X}$	Phasor.

Received 24 October 2024; revised 15 January 2025 and 5 March 2025; accepted 1 April 2025. Date of publication 8 April 2025; date of current version 26 May 2025. This work was supported by the National Key Research and Development Program of China under Grant 2023YFB2407400. Recommended for publication by Associate Editor S. A. Khajehoddin. *(Corresponding authors: Wu Chen; Jiangfeng Wang.)*

Yutong Chen, Wu Chen, Haixi Zhao, Zewei Hao, Jianxi Lan, Xuze Wang, Xin Li, Runyan Sha, Jiangfeng Wang, Xin Li, and Wei Jiang are with the Center for Advanced Power Conversion Technology and Equipment, School of Electrical Engineering, Southeast University, Nanjing 210096, China (e-mail: 220232932@seu.edu.cn; chenwu@seu.edu.cn; 230218870@seu.edu.cn; haozewei@whu.edu.cn; jxlan@seu.edu.cn; 220222704@seu.edu.cn; 220235012@seu.edu.cn; 220235009@seu.edu.cn; jfwang@seu.edu.cn; li-xin@seu.edu.cn; jiangwei@seu.edu.cn).

Yubo Yuan is with the State Grid Jiangsu Electric Power Company Ltd., Research Institute, Nanjing 211103, China (e-mail: yyb@js.sgcc.com.cn).

Color versions of one or more figures in this article are available at https://doi.org/10.1109/TPEL.2025.3558199.

Digital Object Identifier 10.1109/TPEL.2025.3558199

I. INTRODUCTION

WITH the rise of distributed power generation such as wind turbines and photovoltaics, the demand for intelligent power grids has gradually increased [1]. The unstable and unpredictable power output of distributed generation [2] requires the distribution network to achieve flexible power allocation. The impact of distributed power generation may lead to issues such as feeder power imbalance [3], voltage violation [4], and equipment failure. However, traditional methods adopted by existing distribution networks are usually unable to meet the requirements of automation for medium-voltage feeder networks. Devices such as controlling mechanical node switches operate in either ON or OFF states, thereby constraining the adjustment range. Faults and diagnosis procedures may even lead to power outages, affecting the stability and quality of power supply to users. Network reconfiguration in distribution networks is an effective direction to improve grid stability and reliability [5].

The SOP technology, which relies on power electronic equipment, can mitigate voltage unbalance [6], [7], be used for active power flow control [8] and improve the system's robustness [9]. SOP can offer greater control flexibility to enhance system performance [10]. Because the more intrinsic degrees of freedom a topology has, the more flexible its control can be. As illustrated in Fig. 1, unlike traditional mechanical switches, SOP enables continuous power adjustment and rapid switching of operating conditions while maintaining connection to the power grid [11]. By implementing SOP, distributed power sources can be integrated into the existing power grid without the need for upgrades to the infrastructure [12]. SOP allows targeted power transmission [13], regulation of power flow [14], control of power factor, and improvement of voltage distribution [15], thereby significantly enhancing the flexibility, efficiency, and reliability of existing distribution networks.

Typical SOP topologies include BTB-VSC [16], BTB-NPC [17], BTB-MMC [18], and CHB [19]. Currently, BTB-VSC is a classic topology suitable for medium-voltage and low-voltage feeder interconnection [20]. The BTB-VSC output is two-level. Due to limitations in device voltage rating, switching losses,

and harmonic issues, it is not suitable for high-voltage systems. Both BTB-MMC and CHB can regulate power and are suitable for medium-voltage and high-voltage systems. BTB-MMC, however, requires a large number of submodules to handle high voltage, and its submodules can adopt various topologies, such as full-bridge or half-bridge. In cases where both full-bridge and half-bridge MMCs are applicable, the half-bridge-MMC has the higher efficiency and lower device count [21]. However, all MMC topologies require substantial energy storage, typically in the form of submodule capacitors, to reduce submodule voltage ripple [22]. Due to the large number of submodules and substantial energy storage, MMC occupies significant space and incurs high costs. Lan et al. [23] proposed three-phase multiplexing arm MMC by reusing the multiplexing arm for one-third fundamental period, which enhances power density while significantly reducing the number of required submodules and capacitors. A time-sharing principle-based MMC proposed in [24] effectively reduces the required submodules by applying a "time-sharing" principle. However, it cannot be ignored that the referred two topologies still need a large number of capacitors and switches. CHB, another typical SOP, is composed of numerous modules which contain two full bridges and a dc–dc converter. Zhao et al. [25] proposed a shared module SOP based on shared modules, which effectively reduces the number of H-bridge modules compared to traditional CHB-SOP, thus reducing cost. Series–shunt multiport soft normally open points (S^2-MSNOP) proposed in literature [26], has the capability to simultaneously connect multiple feeders with reduced components compared to the traditionally SOP. However, S^2-MSNOP comes at the expense of limiting the operational area of the balance node and the literature does not provide a precise derivation of that operational area.

The successful development and application of high-voltage wide-bandgap semiconductors have opened up new avenues for the evolution of power electronic topologies. High-voltage wide bandgap semiconductors such as SiC exhibit remarkable advantages in high-voltage and high-frequency operating environments [27]. Compared with silicon devices, SiC MOSFETs boast higher switching speeds, lower switching losses, and the ability to withstand high voltage peak stresses, enabling them to operate at higher power levels [28].

Due to above advantages, wide-bandgap semiconductors have been used in several scenarios. The medium-voltage three-level inverter is built by 15-kV SiC IGBTs in literature [29] to meet the requirements of high-voltage applications. In order to leverage the advantages of modular high-voltage wide bandgap semiconductors, Chen et al. [30] designed a megawatt-scale MMC medium-voltage power converter based on 10 kV SiC MOSFET module. In addition, 10 kV SiC MOSFETs are used in [31] to take advantage of the switching speed fully.

This article proposes a novel and compact interconnection topology, DM-SOP, designed for flexible interconnection scenarios in 10 kV distribution networks and 1 MW transmission systems. Given that the dc voltage is set at 6.5 kV [18], the proposed DM-SOP utilizes 10 kV high-voltage SiC MOSFETs. DM-SOP enables bidirectional energy transmission between two feeders with fast active and reactive power flow regulation

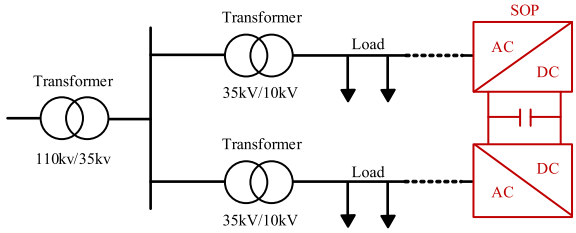

Fig. 1. Schematic diagram of SOP connecting two feeders.

capabilities. This topology is modular and small size for reusing the MM and half bridges, resulting in lower loss and higher efficiency. The DM-SOP is compared to the BTB-VSC, BTB-NPC, and BTB-MMC (Half-bridge) topologies in terms of efficiency, volume, and switch count. The contribution of the article are as follows.

1) A universal topology with multiplexed modules is proposed, along with a dedicated control strategy tailored to its unique structure. The feasibility of the proposed topology is demonstrated through analytical derivation and experimental validation.
2) The operating range of the proposed topology is established through current and voltage phasor analysis. Additionally, a reactive power automatic adjustment strategy is introduced to ensure stable operation across the entire operating range.
3) A comparative analysis with conventional topologies demonstrates a significant reduction in switch count and footprint. This analysis quantitatively validates the improved compactness and efficiency of DM-SOP.

The rest of this article is organized as follows. Description of the topology and operating principle of DM-SOP is presented in Section II. In Section III, the control method and energy balance strategy are derived. Section IV discusses the analysis of DM-SOP's operating range and presents a comparison between different topologies. In Section V, the feasibility verification under medium voltage conditions is conducted and a small-power prototype is constructed. Finally, Section VI concludes this article.

II. Topology and Operating Principle

A. Topology

The topology of DM-SOP, based on high-voltage wide bandgap semiconductor switches, is shown in Fig. 2. The proposed DM-SOP topology connects two ac feeders named Feeder 1 and Feeder 2 in the distribution network through filtering inductors L_1 and L_2, respectively. DM-SOP comprises a MM and a IM, as shown in Fig. 2. IM connects in series with MM. Both MM and IM consist of three legs and a dc capacitor. The DM-SOP is constituted by 24 switches, 4 dc capacitors, and 6 inductors. In Fig. 2, u_{gj1} ($j = A, B, C$) and u_{gj2} represent the three-phase ac voltages of Feeder 1 and Feeder 2, respectively. i_{j1} and i_{j2} represent the three-phase ac current of Feeder 1 and Feeder 2, respectively. i_{j3} represents the current flowing into MM. u_{jl} and u_{jr} represent the midpoint voltage provided by

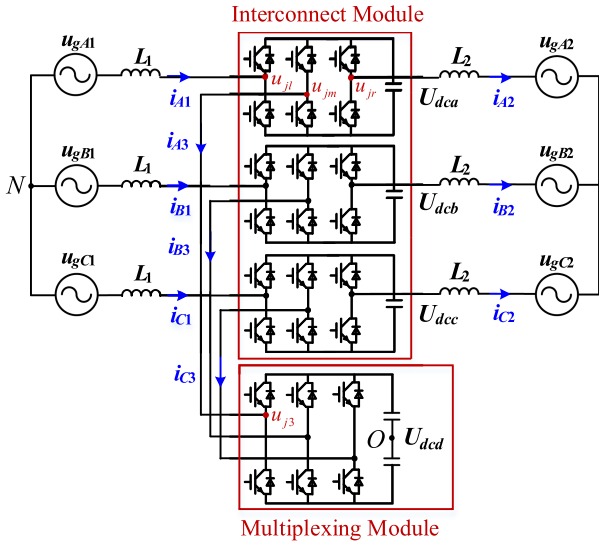

Fig. 2. Topology of DM-SOP.

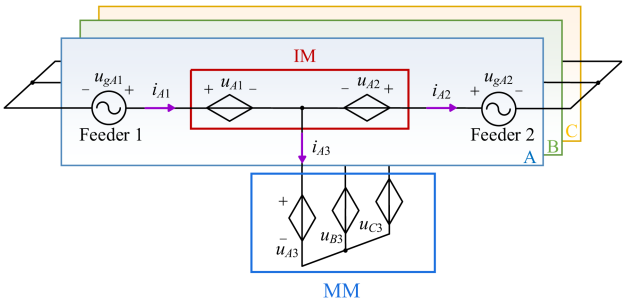

Fig. 3. Equivalent circuit of DM-SOP.

IM for Feeder 1 and Feeder 2, respectively. u_{jm} represents the port voltage provided by the intermediate half-bridge of IM. u_{j3} represents the midpoint voltage of the leg of MM. $U_{\mathrm{dc}\,a}$, $U_{\mathrm{dc}\,b}$, $U_{\mathrm{dc}\,c}$, and $U_{\mathrm{dc}\,d}$ represent the dc capacitor voltages of IM and MM, respectively.

B. Operating Principle

To elucidate the operating principle of DM-SOP, its equivalent circuit is illustrated in Fig. 3. As shown in Fig. 3, the voltages u_{jm} and u_{j3} are multiplexed for both Feeders 1 and 2. u_{j1} represents the voltage provided by the full-bridge of IM at Feeder 1 side, which is equal to $u_{jl} - u_{jm}$. u_{j2} represents the voltage provided by the full-bridge of IM at Feeder 2 side, which is equal to $u_{jr} - u_{jm}$.

According to Fig. 3, it is clear that DM-SOP is composed of two series converters in IM and a parallel converter in MM. DM-SOP multiplexes MM at both input and output sides. The function of the series converters in IM is to control the power flow of both Feeder 1 and Feeder 2. Besides, the function of the parallel converter in MM is to provide port voltages for both Feeder 1 and Feeder 2. The DM-SOP lacks module redundancy, which makes its reliability similar to that of the BTB-VSC. As a result, its reliability is lower than that of the MMC. In the event

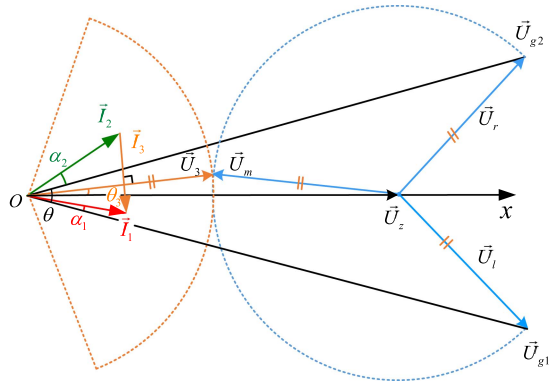

Fig. 4. Phasor diagram of voltage and current.

of a fault, after detecting the abnormal current, DM-SOP can achieve fault isolation by locking all the modules.

Defining the voltage supported by u_{j1} and u_{j3} jointly as u_{j13}, the voltage supported by u_{j2} and u_{j3} jointly can be defined as u_{j23}. u_{j13} represents the port voltage of DM-SOP at Feeder 1, and u_{j23} represents the port voltage of DM-SOP at Feeder 2. Hence, the following expression about the relationships between the port voltages can be obtained:

$$\begin{cases} \vec{U}_{jg1} = \vec{U}_{jL1}+\vec{U}_{j1}+\vec{U}_{j3} \approx \vec{U}_{j1}+\vec{U}_{j3}=\vec{U}_{j13} \\ \vec{U}_{jg2} = -\vec{U}_{jL2}+\vec{U}_{j2}+\vec{U}_{j3} \approx \vec{U}_{j2}+\vec{U}_{j3}=\vec{U}_{j23} \end{cases} \tag{1}$$

where $\vec{U}_{jL1}$ and $\vec{U}_{jL2}$ represent the phasors of the voltage drops across the filtering impedances at Feeder 1 and Feeder 2, respectively.

The voltage drop across the filtering impedance is small compared to the feeder voltages, and the voltage drop across the line impedance is small relative to that across the filtering impedance. To simplify the calculations, the voltage drop across the impedances is neglected in the following derivation. The impact of this assumption will be discussed in Section IV.

Assuming a phase shift of θ between the two feeders and taking the bisector of the angle between their voltage phasors as the 0° reference,, a phasor diagram for both voltage and current in phase A can be drawn, as shown in Fig. 4.

Fig. 4 helps to better understand the relationship between port voltages, as shown in (1). The port voltages of MM and IM need to work together to support the voltage of both feeders.

The current of Feeder 1 leads the voltage of Feeder 1 by a phase α_1, while the current of Feeder 2 leads the voltage of Feeder 2 by a phase α_2. $\vec{U}_z$ is defined as $\vec{U}_3 - \vec{U}_m$ which will be used in the following further derivation. Besides θ_3 represents the phase that the voltage of MM leads bisector of the two feeders, as shown in Fig. 4.

Meanwhile, the energy balance of both MM and IM should be considered. To stabilize the dc capacitor voltage of MM at the reference value $U_{\mathrm{dc}\,ref}$, the phase of u_3 should be controlled, ensuring it is perpendicular to the current i_3. Therefore, the formula (2) can be given as follows:

$$\vec{U}_3 \cdot \vec{I}_3 = 0 \tag{2}$$

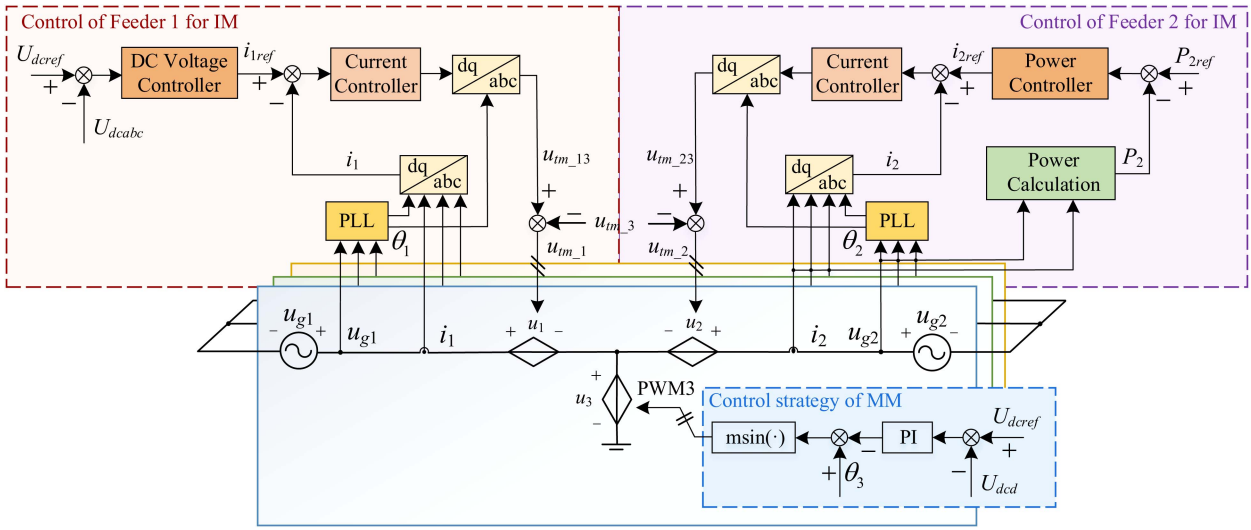

Fig. 5. Overall control block diagram of the topology.

where $\vec{U}_3$ represents the phasor of the port voltage of the MM and $\vec{I}_3$ represents the phasor of the current flowing into MM.

Based on Fig. 4, current equations can be formulated as follows:

$$\vec{I}_1 = \vec{I}_2 + \vec{I}_3 \tag{3}$$

where $\vec{I}_1$ represents the phasor of the current flowing into DM-SOP from Feeder 1 and $\vec{I}_2$ represents the phasor of the current flowing out of DM-SOP from Feeder 2.

III. Control Strategy

The control strategies of DM-SOP include the control strategy of MM as well as the control strategy of IM. The control strategy of MM aims at keeping the voltage of dc capacitor $U_{\mathrm{dc}\,d}$ stable. In order to maintain the energy balance of MM, the phasor of the port voltage $\vec{U}_3$ provided by MM is required to be perpendicular to the current $\vec{I}_3$. The control strategy of IM not only needs to keep energy balance but also to support the voltages of the two feeders. The overall control block diagram of the DM-SOP is shown in Fig. 5. The control strategies for MM and IM are derived below.

A. Control Strategy of MM

The control strategy of MM contains two aspects, controlling the phase and the amplitude of modulation wave u_{tm_3}. According to (2), the phase of u_{tm_3} should be perpendicular to the current i_3. It also means that the energy of MM should be kept balanced to stabilize the voltage of the capacitor. Thus, an outer voltage loop could be taken to control the phase θ_3. The theoretical value of θ_3 can be calculated, and a detailed derivation is provided in Section IV. During operation, θ_3 is dynamically adjusted near the theoretical value. If the voltage $U_{\mathrm{dc}\,d}$ detected is larger than the reference value, it indicates that the capacitor in MM is being charged. Then, the increase of θ_3 is needed. Similarly, if the voltage detected is smaller, θ_3 will be decreased.

Then, the question comes to determine the amplitude of u_{tm_3}, which is closely related to the module voltage $U_{\mathrm{dc}ref}$ and modulation index m. Because DM-SOP has a modular feature, the parameters of each module are the same. In order to ensure the balance of the output of each module in DM-SOP, the port voltage amplitude of each module is designed to be consistent.

To determine the amplitude of u_{tm_3}, the port voltage U_x should be calculated first. As shown in Fig. 4, since the voltage amplitude of each leg of MM and IM is the same, the end of $\vec{U}_z$ must lie on the angle bisector of the voltage of the two feeders. Consequently, the minimum port voltage U_x required by each module and the modulation index m satisfy the following relationships:

$$U_x{=}U_3{=}U_m{=}U_l{=}U_r \le \frac{U_{\mathrm{dc}ref}}{2} \tag{4}$$

$$m = \frac{2U_x}{U_{dcref}} < 1. \tag{5}$$

As long as the control of IM satisfies (1), (2), (4), and (5), it can support both input and output voltages under the balance of each module.

U_x can be calculated according to Fig. 4. Because the end of $\vec{U}_z$ lies on the 0° reference line, U_z can be derived, as shown in

$$U_z = 2U_x \cos\theta_3. \tag{6}$$

Combining (5) and (6), the port voltage U_x required by each module satisfies the following derivation:

$$\left(2U_x\cos\theta_3 - U_{g1}\cos\frac{\theta}{2}\right)^2 + \left(U_{g1}\sin\frac{\theta}{2}\right)^2 = {U_x}^2. \tag{7}$$

The function derived from (7) can be simplified as

$$U_x = \frac{2\cos(\theta_3)\cos\left(\frac{\theta}{2}\right) - \sqrt{1-4\cos^2(\theta_3)\sin^2\left(\frac{\theta}{2}\right)}}{4\cos^2(\theta_3)-1}U_{g1}. \tag{8}$$

From (2), the modulation wave phase θ_3 of the MM can be determined. Combining (5) and (8), amplitude of u_{tm_3} can be

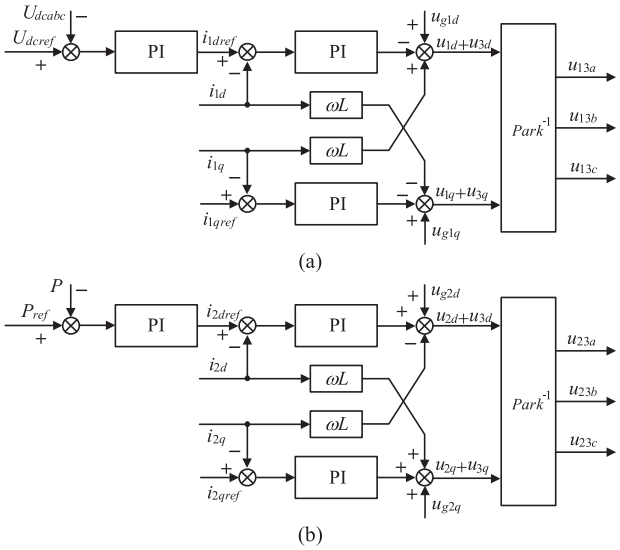

Fig. 6. Control strategy. (a) Voltage balance control of Feeder 1. (b) Power transmission control of Feeder 2.

derived. Hence, the modulation wave u_{tm_3} of MM is derived in (9), and its control block diagram is shown in the control strategy of MM in Fig. 5

$$u_{tm\_3}(t) = \frac{2U_x}{U_{dcref}} \cdot \sin(\omega t + \theta_3). \tag{9}$$

B. Control Strategy of IM

To achieve overall control, it is important to realize energy balance at the input side (Feeder 1) and achieve power control at the output side (Feeder 2). Through above approach, the modulation wave for input side u_{tm_13} and output side u_{tm_23} can be obtained. The input and output hybrid modulation waves are composed of MM's modulation wave u_{tm_3} and IM's modulation waves' u_{tm_1} and u_{tm_2}. Given that the modulation strategy for MM is derived from Section III-A, the modulation wave for IM can be obtained by subtracting the modulation wave of MM u_{tm_3} from the hybrid modulation waves u_{tm_13} and u_{tm_23}, as shown in Fig. 5.

The control block diagrams of both Feeder 1 and 2 side are shown in Fig. 6. The *Park* transformation based on its own phase *A* is performed to obtain the required port voltages u_{13} and u_{23}. The IM connected to Feeders 1 and 2 can be equivalently modeled as two full-bridges, which share the intermediate arm. Similar to the traditional control strategy, as shown in Fig. 6(a), *dq* vector control is applied to the rectifier connected to Feeder 1 to maintain the voltage of the dc capacitor in the IM. The outer loop control of the inverter connected to Feeder 2 regulates the power and generates the current reference, as shown in Fig. 6(b).

U_z can be obtained through (6) and the phase of $\vec{U}_z$ is 0 degrees. Therefore, u_z can be expressed as follows, where ω is defined as the angular frequency:

$$u_z(t) = 2U_x \cos(\theta_3) \sin(\omega t). \tag{10}$$

As depicted in Fig. 4, the midpoint voltage of the intermediate leg of IM $\vec{U}_m$ points from the end of $\vec{U}_z$ to the end of $\vec{U}_3$.

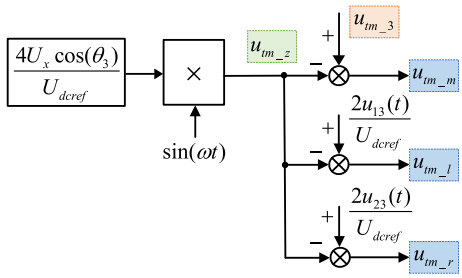

Fig. 7. Control strategy of IM.

According to (9) and (10), the modulation wave u_{tm_m} of IM's intermediate leg can be expressed as follows:

$$\begin{aligned} u_{tm\_m}(t) &= -u_z(t)\frac{2}{U_{dcref}} + u_{tm\_3}(t) \\ &= -\frac{4U_x\cos(\theta_3)}{U_{dcref}}\sin(\omega t) + \frac{2U_x}{U_{dcref}} \cdot \sin(\omega t + \theta_3). \end{aligned} \tag{11}$$

Based on the control strategy shown in Fig. 6, after determining port voltages u_{13} and u_{23}, the modulation waves u_{tm_l} and u_{tm_r} can be identified according to Fig. 7 and (10)

$$u_{tm\_l}(t) = [u_{13}(t) - u_z(t)]\frac{2}{U_{dcref}} \tag{12}$$

$$u_{tm\_r}(t) = [u_{23}(t) - u_z(t)]\frac{2}{U_{dcref}}. \tag{13}$$

Using (11) (12), and (13), the modulation waves for u_{tm_l}, u_{tm_m}, and u_{tm_r} can be obtained, as illustrated in Fig. 7. In summary, the modulation waves for all arms of the DM-SOP can be obtained.

IV. Operating Range and Comparison

A. Operating Range

The connection scenario is set to use 10 kV SiC MOSFETs to connect two 10 kV feeders and take θ as 30° as the worst situation. Considering the voltage withstand capability of the switching components, U_{dcref} is set at 6.5 kV[18]. Following derivation is based on above data. Therefore, the port voltage U_x can be determined according to (8) and the relationship between U_x, θ_3 as well as θ is shown as in Fig. 8.

There is no denying that U_x grows with the increase of $|\theta|$. When θ is considered as a specific value, U_x is solely affected by the magnitude of $|\theta_3|$. The operating range of DM-SOP is mainly affected by θ_3 of MM because it will influence whether the port voltages of DM-SOP can support the voltages of feeders. So it is important to figure out the range of the modulation offset angle θ_3 of MM, which is determined by the active power *P*, the reactive power Q_1 as well as Q_2.

To begin with, the function about the value of θ_3 can be derived from (8) as follows:

$$\cos\theta_3 = \frac{U_{g1}}{2U_x}\cos\left(\frac{\theta}{2}\right) - \frac{1}{2}\sqrt{1 - \left(\frac{U_{g1}}{U_x}\right)^2 \sin^2\left(\frac{\theta}{2}\right)}. \tag{14}$$

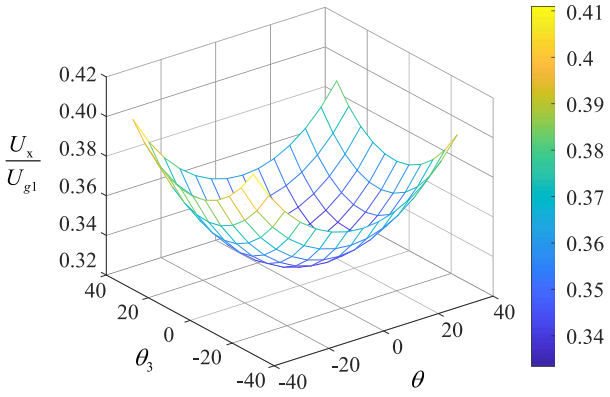

Fig. 8. Relationship between U_x, θ_3 as well as θ.

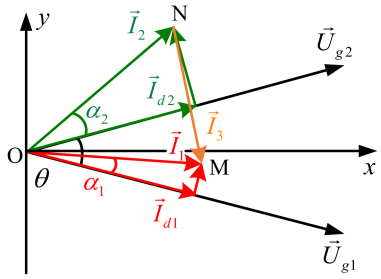

Fig. 9. Current phasor diagram.

It can be clearly seen from (14), with the rise of the required port voltage U_x, $|\theta_3|$ increases. And from (5), it is obvious that U_{g1}/U_x should be larger than $2U_{g1}/U_{\mathrm{dc}ref}$. Therefore the range of θ_3 can be determined. In the mentioned 10 kV feeder connection scenario with $U_{\mathrm{dc}ref}$ set at 6.5 kV, $2U_{g1}/U_{\mathrm{dc}ref}$ equals to 2.51, thus, the relationship between θ_3 and θ is clear. With the rise of θ, the range of θ_3 decreases. If take θ as 30° as the worst situation, θ_3 can change from about −34° to 34°, thus taking the adjustment range of θ_3 between −30° to 30° would be appropriate

$$-30^\circ \le \theta_3 \le 30^\circ. \tag{15}$$

After determining the adjustment range of θ_3, it is important to figure out the influence of power flow have on θ_3. When Feeder 1 absorbs inductive reactive power and Feeder 2 generates inductive reactive power under the control of DM-SOP, the current phasor diagram is shown in Fig. 9, where i_{d1} represents the d-axis component of the current of Feeder 1, and i_{d2} represents the d-axis component of the current of Feeder 2.

The relationships between α_1, α_2 , P, Q_1, and Q_2 are shown in

$$\tan\alpha_1 = \frac{Q_1}{P}, \tan\alpha_2 = -\frac{Q_2}{P}. \tag{16}$$

The maximum reactive power capability is designed at 30% of the active power capability. Hence, the range of tanα_1 and tanα_2 are shown as follows:

$$\begin{cases} -0.3 \le \tan\alpha_1 \le 0.3 \\ -0.3 \le \tan\alpha_2 \le 0.3 \end{cases}. \tag{17}$$

TABLE I
OPERATIONAL CASES ANALYSIS

1	2	3	4	5
Q_1=0	Q_1>0	Q_1>0	Q_1<0	Q_1<0
Q_2=0	$Q_2 \ge 0$	$Q_2 \le 0$	$Q_2 \ge 0$	$Q_2 \le 0$
α_1=0	α_1>0	α_1>0	α_1<0	α_1<0
α_2=0	$\alpha_2 \le 0$	$\alpha_2 \ge 0$	$\alpha_2 \le 0$	$\alpha_2 \ge 0$
Fig. 10(a)	Fig. 10(b)	Fig. 9	Fig. 10(c)	Fig. 10(d)

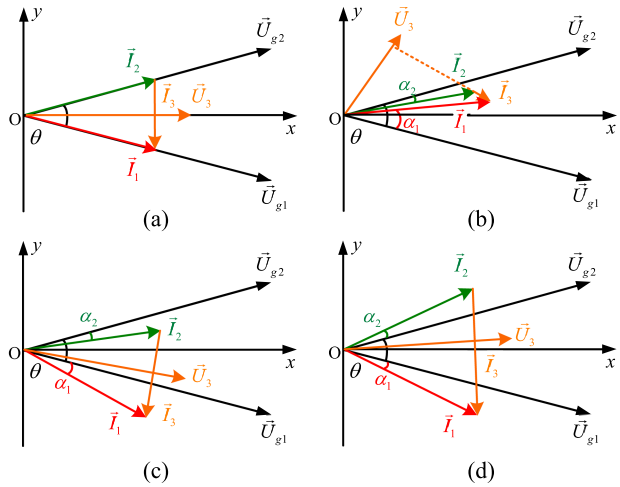

Fig. 10. Current phasor diagram of different cases. (a) Q_1=0, Q_2=0, α_1=0, α_2=0; (b) Q_1>0, Q_2≥0, α_1>0, α_2≤0; (c) Q_1<0, Q_2≥0, α_1<0, α_2≤0; (d) Q_1<0, Q_2≤0, α_1<0, α_2≥0.

Based on the different values of Q_1 and Q_2, the following cases can be classified, as shown in Table I, with the corresponding voltage phasor diagrams illustrated in Figs. 9 and 10.

Fig. 10(a) illustrates Case 1 in Table I, where under the control of DM-SOP, both feeders operate in a unity power factor mode. Fig. 10(b) represents the scenario of Case 2 in Table I, both the input and output feeders are absorbing inductive reactive power, resulting in similar magnitudes and phases of the input and output currents. In Fig. 10(c), Feeder 1 is working under the case of generating inductive reactive power while Feeder 2 is working under the case of absorbing inductive reactive power. In Fig. 10(d), both Feeders 1and 2 generate inductive reactive power, and the phase of u_3 deviates slightly from the bisector.

Among above situations, working with similar currents of Feeder 1 and Feeder 2 may result in the rise of $|\theta_3|$ like Fig. 10(b). Thus, the operation range is influenced by the currents, which are ultimately due to the power flow. The following content will conduct theoretical derivation and calculation for the operating range. Since the input and output active powers are conserved, the voltage magnitudes of the two feeders are approximately equal, the relationship between the active currents of the two feeders can be derived as follows:

$$I_{d1} = I_{d2} = I_d. \tag{18}$$

According to the preliminary active and reactive power distribution, the amplitude and phase of currents flowing through Feeder 1 and Feeder 2 can be obtained from Fig. 9 and (18) as

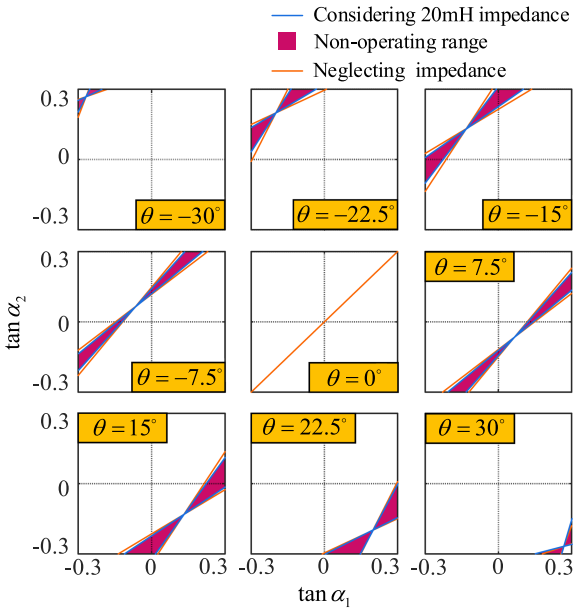

Fig. 11. Operation range with different θ.

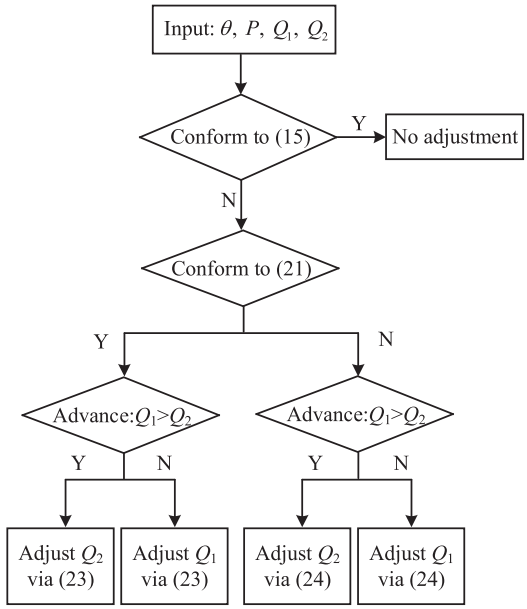

Fig. 12. Automatic adjustment algorithm of reactive power.

follows:

$$\begin{cases} I_1{=}OM{=}\frac{I_d}{\cos(\alpha_1)}, \angle I_1 = -\frac{\theta}{2} + \alpha_1 \\ I_2{=}ON{=}\frac{I_d}{\cos(\alpha_2)}, \angle I_2 = \frac{\theta}{2} + \alpha_2. \end{cases} \tag{19}$$

Thus, the phase of $\vec{U}_3$ can be deduced as follows:

$$\theta_3 = \arctan\left(\frac{\tan\alpha_1 + \tan\alpha_2}{2 - \frac{\tan\alpha_1 - \tan\alpha_2}{\tan\frac{\theta}{2}}}\right). \tag{20}$$

If θ_3 does not satisfy (15), it may fall into two cases as shown in (21) and (22).

$$\tan\theta_3 \geq \frac{1}{\sqrt{3}} \text{if} \tan\theta_3 \geq 0 \tag{21}$$

$$\tan\theta_3 \leq -\frac{1}{\sqrt{3}} \text{if} \tan\theta_3 < 0. \tag{22}$$

To be more concrete, the range of $\tan\alpha_1$ and $\tan\alpha_2$ that satisfy (21) and (22) is the area enclosed by the orange lines in Fig. 11, which is defined as the nonoperating range. The nonoperating range represents the region where the DM-SOP fails to operate. Thus a reactive power automatic adjustment strategy will be introduced in the following part. The above derivation simplifies the analysis by neglecting the voltage drop across the filtering inductance and line inductance, as mentioned in Section II. To demonstrate that the impact of inductive voltage drop is minimal, the operating range with a 20 mH inductive voltage drop is plotted. The nonoperating range, considering the inductive voltage drop, is the area enclosed by the blue lines and highlighted in pink. As can be seen from Fig. 11, except for $\theta = 30°$, in other cases, the nonoperating range becomes slightly smaller after considering the inductive impedance. When $\theta = 30°$, the nonoperating range is slightly larger than the original range. However, since the original nonoperating range already has a certain margin, the impact is negligible.

B. Reactive Power Automatic Adjustment Strategy

According to the analysis above, the operating range of DM-SOP has been calculated via (21) and (22). If the power flow of Feeder 1 and Feeder 2 falls within the nonoperating range, DM-SOP may fail to operate. To ensure the normal operation of DM-SOP, the power flow control order given to the DM-SOP will undergo the following automatic reactive power adjustment.

If the preliminary active and reactive power distribution satisfies (15)–(17) and (20), DM-SOP can operate correctly with the given values. However, if the initial power distribution does not satisfy (15), an automatic adjustment of reactive power demand will be triggered. There is a priority between reactive power Q_1 and Q_2. If Q_1 has higher priority, Q_2 will be adjusted to satisfy (15) and ensure the normal operation of DM-SOP. If Q_2 has higher priority, Q_1 will be adjusted instead.

The block diagram of the automatic reactive power adjustment algorithm is shown in Fig. 12. For example, if the preliminary P, Q_1, Q_2, and θ do not satisfy (15), which is necessary for the normal operation of DM-SOP, the algorithm checks whether they satisfy (21). If (21) is satisfied, it means that θ_3 will be fixed to the maximum adjustment angle of 30° to ensure the normal operation. The adjustment of θ_3 is driven by the adjustments of Q_1 or Q_2 from the root. Therefore, the following function is derived based on (20). This condition ensures that after adjustment of either Q_1 or Q_2, the values of P, Q_1, Q_2, and θ satisfy (23) to maintain θ_3 at 30°

$$\left(\sqrt{3}\tan\frac{\theta}{2} + 1\right)Q_1 + \left(\sqrt{3}\tan\frac{\theta}{2} - 1\right)Q_2 = 2P\tan\frac{\theta}{2}. \tag{23}$$

If (21) is not satisfied, it means that θ_3 will be fixed to $-30°$. Similarly, the relationship between P, Q_1, Q_2, and θ after

TABLE II
COMPARISON BETWEEN TOPOLOGIES

Typology	DM-SOP	BTB-VSC	BTB-NPC	BTB-MMC
Number of 10 kV, 120 A SiC MOSFETS	12	36	36	/
Number of 10 kV, 90 A SiC MOSFETS	/	/	/	72
Number of 10 kV, 60 A SiC MOSFETS	12	/	/	/
Number of capacitors	4	1	2	36
Voltage of capacitors/kV	6.5	18	9	6
Capacitance/mF	0.40	0.20	0.50	0.20
Capacitor volume/m^3	0.305	0.310	0.435	1.175
Number of inductors	6	6	6	6/12
Inductance/mH	19	38	18	8.5/47
Peak current of inductors/A	81.65	81.65	81.65	81.65/59.35
Inductor volume/ m^3	0.637	1.273	0.603	1.949

adjustment can be derived as follows:

$$\left(1-\sqrt{3}\tan\frac{\theta}{2}\right)Q_1-\left(\sqrt{3}\tan\frac{\theta}{2}+1\right)Q_2=2P\tan\frac{\theta}{2}. \tag{24}$$

Assuming that (21) is satisfied, if Q_1 has higher priority, Q_2 will be adjusted according to (23) to ensure that θ_3 equals 30°, and vice versa. Intuitively, if the initial power falls within the nonoperating range shown in Fig. 11, the above algorithm can adjust it to the feasible region while making the least adjustment to the reactive power. Which side of the reactive power will be adjusted depends on the priority set manually.

The aforementioned automatic adjustment strategy ensures the operation of the topology under the different scenarios listed in Table I, with minimal impact on the adjustments. Although the proposed control strategy can automatically adjust the power factor to ensure the operation of the topology, there remains a range in which the system cannot operate.

C. Compared With Other Topologies

As shown in Fig. 4, the multiplexing module voltage $\vec{U}_3$ of the DM-SOP, together with the intermediate bridge arm voltage $\vec{U}_m$, jointly support the two feeder voltages, significantly reducing the number of components compared to other topologies. To better highlight the advantages of DM-SOP, different topologies using the same 10 kV SiC MOSFET are considered in the context of connecting two 10 kV feeders while transmitting 1 MW.

Table II compares the DM-SOP, BTB-VSC, BTB-NPC, and BTB-MMC in terms of the number of MOSFETs, as well as the number, voltage rating, capacitance, and volume of capacitors, and the number, current rating, inductance, and volume of inductors.

For switches that carry a maximum current of 81.65 A, SiC switches with a voltage rating of 10 kV and a current rating of 120 A can be selected. In the case of DM-SOP, the current flowing out of the IM's middle bridge arm is the same as the current flowing into the MM. When θ equals 30°, the current magnitude under rated conditions is approximately 42.2 A, so switches with a current rating of 60 A can be selected. For the MMC, the current through each switch consists of an ac component with an amplitude of 40.8 A and a dc component of 18.5 A, resulting in a peak current of approximately 59.35 A. Therefore, 10 kV, 90 A MOSFETs can be used. For different topologies, the quantities of the different types of switches required are summarized in Table II and Fig. 13.

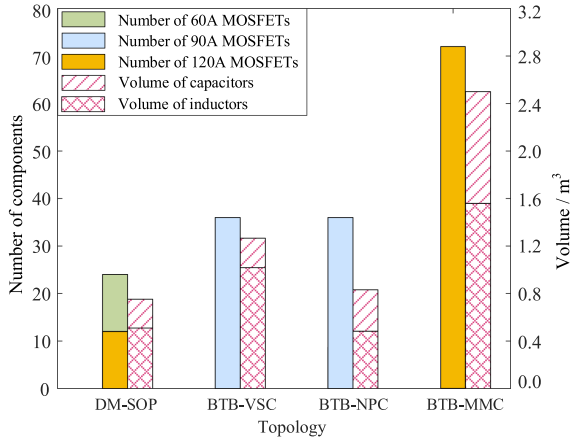

Fig. 13. Numbers of MOSFETs and the volume of topologies.

For SOP with common dc bus, such as BTB-VSC, BTB-NPC, and BTB-MMC, the dc bus voltage should be at least 18 kV with modulation index m set to 0.9. Hence, both the upper and lower arms of the BTB-VSC require at least three MOSFETs connected in series to withstand the dc bus voltage. As a result, 36 MOSFETs as well as 6 inductors are needed for BTB-VSC. For BTB-NPC, two capacitors with dc voltage rated for 9 kV are required. To withstand the dc voltage, the first and forth MOSFETs in one arm are composed of two MOSFETs connected in series. With 6 MOSFETs in one arm, the BTB-NPC consists of 36 MOSFETs and 6 filter inductors. For a BTB-MMC using half bridge submodules, considering the 10 kV voltage rating of the MOSFETs, the total number of upper and lower arm submodules in one phase is designed to be 6. Thus, the voltage of the submodule capacitor is rated for 6 kV. This means the total number of MMC submodules is 36, consisting of 36 capacitors, 72 switches, 6 filter inductors, and 12 arm inductors. For all filter inductors of the topologies, the peak current remains consistent at 81.65 A. In contrast, the peak current for the arm inductors in the MMC is 59.35 A.

As can be seen from Table II, it is evident that the DM-SOP topology significantly reduces the number of required switches compared to other topologies by multiplexing submodules. The required capacitance value to limit the dc voltage fluctuation within 5% are shown in Table II [32], [33]. To estimate the volume of each topology, capacitors of the same model,

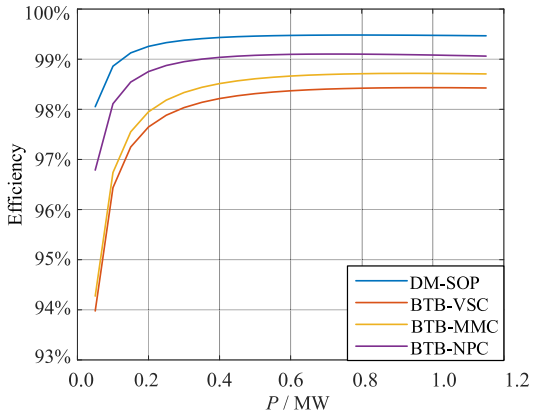

Fig. 14. Efficiency of topologies.

TABLE III
SIMULATION PARAMETERS

Parameters	Symbol	Value
Input-side ac voltage	u_{g1}	$10\angle 0°$ kV
Output-side ac voltage	u_{g2}	$10\angle 30°$ kV
System frequency	f	50 Hz
Capacitor voltage of MM and IM	U_{dcref}	6500 V
Capacitance of MM and IM	C	0.4 mF
Input and output filter inductance	L	20 mH
Switching frequency	f_s	10 kHz

B25645A1138K013, are selected. The selection criteria for the inductance value are based on the bilateral Fourier decomposition [34], [35], calculating the port voltage to ensure that the current THD is less than 2%. For the inductors, the effective core volume is calculated to reflect the volume of inductors. As a result, the volume of the capacitors and inductors for each topology are shown in Table II and Fig. 13. Due to the shared port voltage in the DM-SOP, the capacitor requirements are smaller compared to traditional topologies. In contrast, the MMC has the largest capacitor size and inductor size because it involves a higher number of submodules and additional arm inductors.

All topologies transmit 1 MW of power with switching frequencies set at 10 kHz. The DM-SOP demonstrates the highest efficiency, as shown in Fig. 14, after calculating the conduction and switching losses based on the parameters from reference [36]. This is because the DM-SOP uses the fewest switches, resulting in lower loss. As a result, the DM-SOP topology also requires the smallest heatsink volume.

Based on the above data, DM-SOP significantly reduces the number of switches required. In addition, it has advantages in terms of small volume and high efficiency.

V. SIMULATION AND EXPERIMENTAL VALIDATION

A. Simulation Verification

To validate the correctness of the DM-SOP and control strategies, a 10 kV/1MW three-phase flexible interconnection system that employed a discrete solver setting is built in MATLAB/Simulink. The parameters are listed in Table III and the parameters of the 10 kV SiC MOSFETs are set according to [36]. P and Q are calculated based on the voltage and current sampling shown in Fig. 5.

TABLE IV
OPERATION CASES

Cases	Time/s	P_1/p.u.	Q_1/p.u.	P_2/p.u.	Q_2/p.u.
Case 1	0–0.1	0.5	0	–0.5	0
Case 2	0.1–0.2	–0.8	0	0.8	0
Case 3	0.2–0.3	–0.8	–0.1	0.8	–0.2
Case 4	0.3–0.4	–0.8	0.24	0.8	0.18

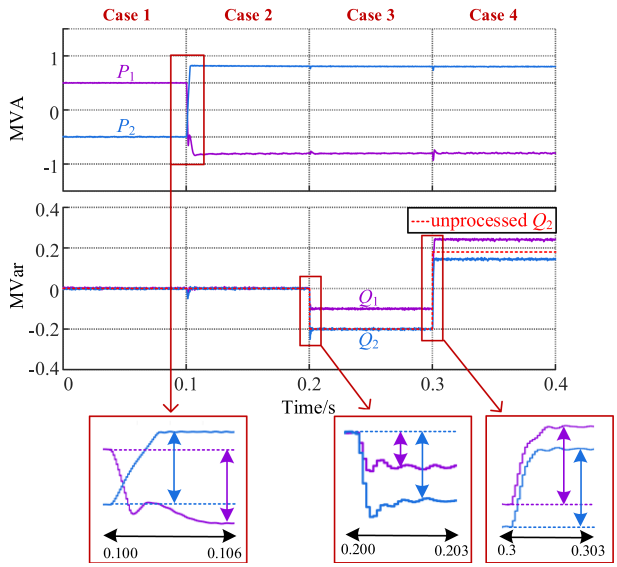

Fig. 15. Active and reactive power curves under four operation cases.

DM-SOP implements the reactive power automatic adjustment strategy proposed in Section IV, with the assumption that Feeder 1 has a higher priority than Feeder 2. Four cases are designed, as shown in Table IV. Case 1 and 2 are intended to verify the bidirectional power transfer capability of DM-SOP. Case 3 and 4 are designed to assess the system's ability to track active and reactive power commands in a timely manner and to perform automatic reactive power adjustment, ensuring that the topology operates effectively under various conditions.

As shown in Fig. 15, in Case 1, during 0–0.1 s, DM-SOP transfers 0.5 p.u. active power from Feeder 2 to Feeder 1. In Case 2, the power is reversed, during 0.1–0.2 s, DM-SOP transfers 0.8 p.u. active power from Feeder 1 to Feeder 2. In Cases 3 and 4, to verify the reactive compensation capability of DM-SOP, the active power transfer is kept unchanged. During 0.2–0.3 s, Feeder 1 provides 0.1 p.u. reactive power while Feeder 2 consumes 0.2 p.u. reactive power under the control of DM-SOP. And during 0.3–0.4 s, Feeder 1 is set to consume 0.24 p.u. reactive power while Feeder 2 is set to provide 0.18 p.u. reactive power.

The currents under the four corresponding operating cases are shown in Fig. 16, along with corresponding THD parameters. The voltage of Feeder 2 leads the voltage of Feeder 1 by 30°. From 0 s to 0.1 s, Feeder 2 transmits 0.5 p.u. active power to Feeder 1, and both Feeder 1 and 2 operate at a unity power factor, with a current amplitude of 40.8 A. At 0.1 s, the power transmission reverses, with Feeder 1 transmitting 0.8 p.u. active power to Feeder 2. The current reverses its phase and increases in amplitude to 65.28 A. The current tracking under the power

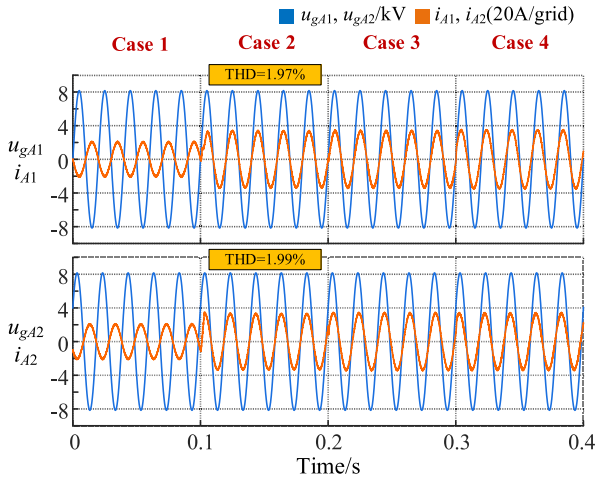

Fig. 16. Voltage-current curves under four operation cases.

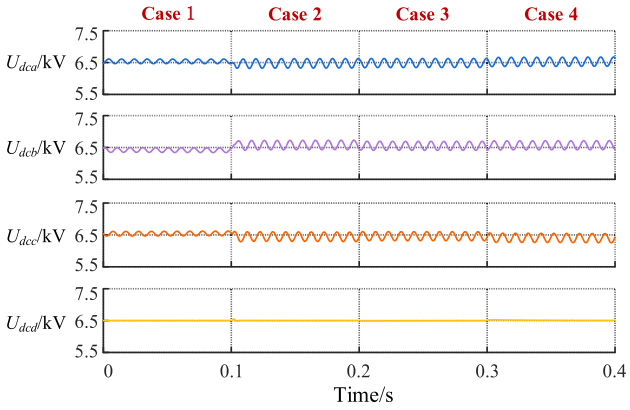

Fig. 17. DC voltage fluctuations of four modules under four operation cases.

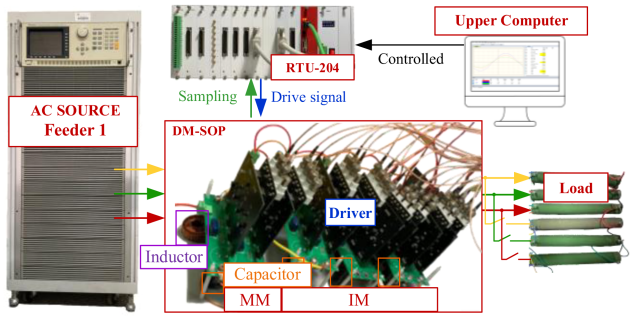

Fig. 18. Experiment system of DM-SOP.

TABLE V
EXPERIMENTAL PARAMETERS

Parameters	Symbol	Value
Input-side ac voltage	u_{g1}	$110\angle 0°$ V
Output-side ac voltage	u_{g2}	$110\angle 30°$ V
System frequency	f	50 Hz
Capacitor voltage of MM and NMM	U_{dcref}	140 V
Capacitance of NM and NMM	C	1 mF
Input and output filter inductance	L	7 mH
Switching frequency	f_s	10 kHz

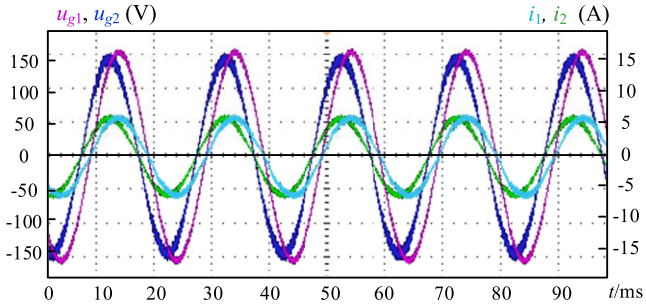

Fig. 19. Voltage and current waveform.

jump takes approximately a quarter of a cycle, indicating good dynamic response. During 0.2 s to 0.3 s, the currents of Feeder 1 and 2 lag the voltage in phase according to the input value of P, Q_1, and Q_2 because at this time (15) is met. During 0.3 s to 0.4 s, the reactive power adjustment strategy works because at the moment, the input value of P, Q_1, and Q_2 would lead to θ_3 equaling 61.52°, thus failing to meet (15). Given that Q_1 owns higher priority, Q_2 is adjusted according to Fig. 12 to ensure the normal operation of DM-SOP. The success of the strategy can be seen from Fig. 15, Q_2 is changed to 0.144 automatically during 0.3 s to 0.4 s, while during 0–0.3 s, Q_2 needs no change.

The dc voltage under four operation cases are depicted in Fig. 17. As the feeder current increases, the second-order harmonic fluctuation of the dc voltage of IM gradually intensifies. Both the voltages of MM and IM remain stable at the reference value of 6.5 kV, which is consistent with the theoretical calculations.

In summary, the feasibility of the DM-SOP topology and control strategy has been verified through simulations. The quality of the current is satisfactory. DM-SOP enables bidirectional energy transfer, active and reactive power decoupling control and exhibits excellent dynamic response characteristics.

B. Experimental Verification

To verify the correctness and feasibility of the proposed power control and energy balance control, a low-power experimental prototype was constructed for principal validation. This article presents the construction of a 1.5 kVA ac three-phase prototype using RTU-204 as the controller and Chroma Programmable AC SOURCE 61511 as the feeder, as illustrated in Fig. 18 and the experimental parameters shown in Table V. C3M0120065D made by Wolfspeed are used in the experiment. The load module contains six resistors, each with a resistance of 50 Ω. The output three phases of DM-SOP are connected to three of these 50 Ω resistors. The remaining three resistors are connected in parallel with the first three, respectively, through circuit breaker, to create conditions for load jumps in the experiment.

Fig. 19 shows the voltage and current waveforms. The amplitude of voltage u_{g1} is $110\sqrt{2}$ V. At this time, the input current is in phase with the input voltage. Meanwhile the amplitude of voltage u_{g2} is $110\sqrt{2}$ V, and the output current is in phase with the output voltage. Both the voltage and current of Feeder 2 leads those of Feeder 1 by 30° in phase. Fig. 20, from top to bottom, represents the dc voltages of the IM and MM. All of them are stabilized at the set value of 140 V.

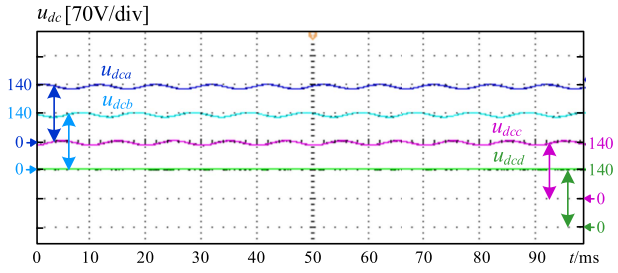

Fig. 20. IM/MM DC voltage waveform.

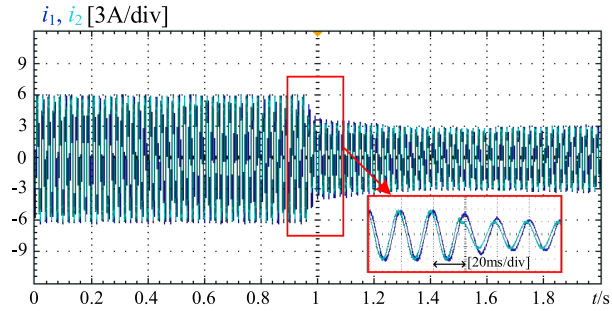

Fig. 21. Current waveform during the load transition from 25 to 50 Ω.

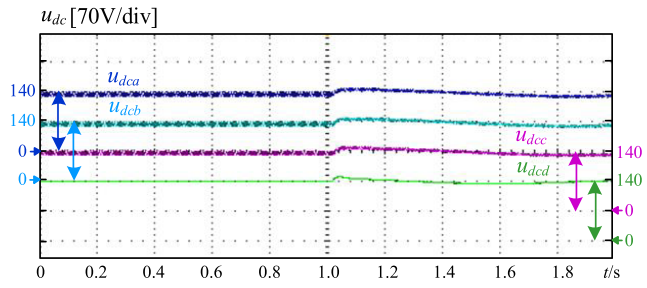

Fig. 22. DC voltage waveform during the load transition from 25 to 50 Ω.

The above experiments have verified the feasibility of the proposed topology and control strategy. To validate the dynamic performance of the system, load jump experiments were conducted. The load was initially set at 25 Ω per phase and then jumped to 50 Ω, and finally jumped back to 25 Ω.

As shown in Fig. 21, in the process of transitioning the load from 25 to 50 Ω, the current drops from 6 to 3 A. Before and after the jump, the current of Feeder 2 maintains 30° lead over the current of Feeder 1, with a dynamic time approximately equal to half a cycle. During the load transition, the voltages of both MM and IM stay around the set value of about 140 V with slight fluctuations, as shown in Fig. 22.

Fig. 23 illustrates the process of the load transitioning back from 50 to 25 Ω. It can be observed from the figure that the current jumps from 3 to 6 A, while the output side current maintains 30° lead over the input side current before and after the transition. The dynamic time of this transition is approximately half a cycle. During the load transition, the voltages of both MM and IM stay around the set value of about 140 V with slight fluctuations, as shown in Fig. 24.

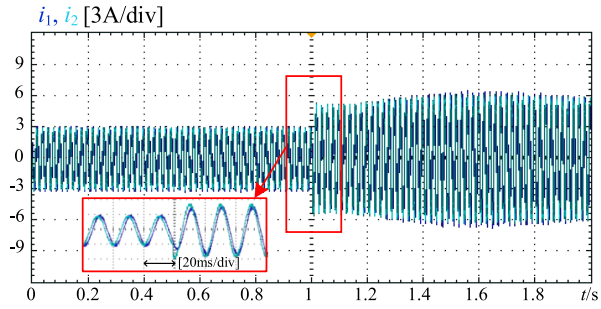

Fig. 23. Current waveform during the load transition from 25 to 50 Ω.

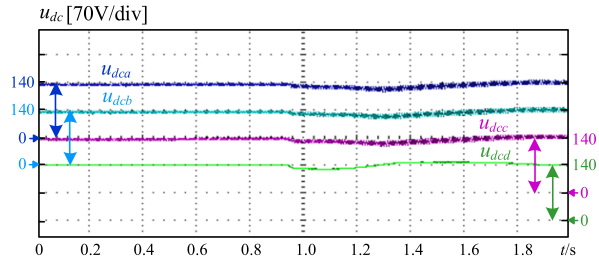

Fig. 24. Dc voltage waveform during the load transition from 25 to 50 Ω.

The aforementioned experiments have validated the stability capability of the outer loop at both input and output sides, as well as the dynamic tracking performance of the current inner loops.

VI. Conclusion

Traditional SOP topologies typically consist of numerous submodules, making them bulky and costly. To address these challenges in medium-voltage distribution networks, this article proposes a dual multiplexing SOP topology based on high-voltage SiC MOSFETs. The proposed topology significantly reduces the number of switches and volume, enhancing efficiency and having advantages in thermal management. Besides, it enables fault isolation. These characteristics make the proposed topology particularly suitable for space-constrained scenarios that require backup energy supply, flexible interconnection or distributed power integration. Although the proposed control strategy can automatically adjust the power factor to ensure the operation of the topology, there remains a range in which the system cannot operate. The high cost and electromagnetic interference of 10 kV SiC switches remains a limitation. Nevertheless, with continued advancements in SiC device research, the cost of 10 kV SiC switches is expected to decrease, facilitating broader adoption and application of the proposed topology.

References

[1] A. Singhal and V. Ajjarapu, "Impact assessment and sensitivity analysis of distribution systems with DG," in *Proc. North Amer. Power Symp.*, 2015, pp. 1–6.

[2] E. Hu, Z. Wang, H. Zhao, J. Guo, and H. Yang, "A novel control strategy to smooth power fluctuation of hybrid offshore wind and tidal power generation system," in *Proc. IEEE Conf. Energy Internet Energy Syst. Integration*, 2017, pp. 1–4.

[3] S. Eftekharnejad, V. Vittal, G. T. Heydt, B. Keel, and J. Loehr, "Impact of increased penetration of photovoltaic generation on power systems," *IEEE Trans. Power Syst.*, vol. 28, no. 2, pp. 893–901, May 2013.

[4] Y. Chai, L. Guo, C. Wang, Y. Liu, and Z. Zhao, "Hierarchical distributed voltage optimization method for HV and MV distribution networks," *IEEE Trans. Smart Grid*, vol. 11, no. 2, pp. 968–980, Mar. 2020.
[5] T. Asakura, T. Genji, T. Yura, N. Hayashi, and Y. Fukuyama, "Long-term distribution network expansion planning by network reconfiguration and generation of construction plans," *IEEE Trans. Power Syst.*, vol. 18, no. 3, pp. 1196–1204, Aug. 2003.
[6] P. Li et al., "Optimal operation of soft open points in active distribution networks under three-phase unbalanced conditions," *IEEE Trans. Smart Grid*, vol. 10, no. 1, pp. 380–391, Jan. 2019.
[7] M. B. Shafik, G. I. Rashed, and H. Chen, "Optimizing energy savings and operation of active distribution networks utilizing hybrid energy resources and soft open points: Case study in Sohag, Egypt," *IEEE Access*, vol. 8, pp. 28704–28717, 2020.
[8] R. You and X. Lu, "Voltage unbalance compensation in distribution feeders using soft open points," *J. Modern Power Syst. Clean Energy*, vol. 10, no. 4, pp. 1000–1008, Jul. 2022.
[9] F. Sun, J. Ma, M. Yu, and W. Wei, "Optimized two-time scale robust dispatching method for the multi-terminal soft open point in unbalanced active distribution networks," *IEEE Trans. Sustain. Energy*, vol. 12, no. 1, pp. 587–598, Jan. 2021.
[10] I. Konstantelos, S. Giannelos, and G. Strbac, "Strategic valuation of smart grid technology options in distribution networks," *IEEE Trans. Power Syst.*, vol. 32, no. 2, pp. 1293–1303, Mar. 2017.
[11] J. M. Bloemink and T. C. Green, "Increasing photovoltaic penetration with local energy storage and soft normally-open points," in *Proc. IEEE Power Energy Soc. Gen. Meeting*, 2011, pp. 1–8.
[12] J. M. Bloemink and T. C. Green, "Increasing distributed generation penetration using soft normally-open points," in *Proc. IEEE PES Gen. Meeting*, 2010, pp. 1–8.
[13] H. Peng et al., "System parameter design method based on a serial-shunt type soft normally open point," in *Proc. 11th Int. Conf. Power Electron. ECCE Asia*, 2023, pp. 2259–2264.
[14] F. Katiraei and J. R. Agüero, "Solar PV integration challenges," *IEEE Power Energy Mag.*, vol. 9, no. 3, pp. 62–71, May/Jun. 2011.
[15] S. K. Chaudhary, J. M. Guerrero, and R. Teodorescu, "Enhancing the Capacity of the AC distribution system using DC interlinks—A step toward future DC grid," *IEEE Trans. Smart Grid*, vol. 6, no. 4, pp. 1722–1729, Jul. 2015.
[16] F. Xu, Y. Lu, L. Li, C. Wang, C. Ding, and M. Zheng, "Research on zero-sequence control strategy of flexible multi-state switch based on transformerless VSC-MVDC," in *Proc. 8th Renewable Power Gener. Conf.*, 2019, pp. 1–6.
[17] V. N. Jakka et al., "Voltage balancing of series connected clamping diodes in medium voltage NPC converter enabled by Gen-3 10 kV SiC MOSFETs for asynchronous micro-grid power conditioning system (AMPCS)," in *Proc. IEEE Energy Convers. Congr. Expo.*, 2019, pp. 5798–5804.
[18] C. Nie et al., "A 13.8 kV, 100 kVA multi-functional MMC-based asynchronous microgrid power conditioning system with 10 kV SiC MOSFETs," in *Proc. IEEE Appl. Power Electron. Conf. Expo.*, 2021, pp. 2229–2236.
[19] H. Akagi and R. Kitada, "Control and design of a modular multilevel cascade BTB system using bidirectional isolated DC/DC converters," *IEEE Trans. Power Electron.*, vol. 26, no. 9, pp. 2457–2464, Sep. 2011.
[20] Z. Ma, K. Fu, Y. Hao, Z. Fang, and S. Li, "Analysis of AC/DC side harmonic interaction of back-to-back VSC based SNOP," in *Proc. IEEE/IAS Ind. Commercial Power Syst. Asia*, 2021, pp. 22–27.
[21] C. T. Collins and T. C. Green, "Comparative analysis of an MV neutral point clamped AC-CHB converter with DC fault ride-through capability," *IEEE Trans. Ind. Electron.*, vol. 67, no. 4, pp. 2834–2843, Apr. 2020.
[22] M. M. C. Merlin, T. C. Green, P. D. Mitcheson, F. J. Moreno, K. J. Dyke, and D. R. Trainer, "Cell capacitor sizing in modular multilevel converters and hybrid topologies," in *Proc. 16th Eur. Conf. Power Electron. Appl.*, 2014, pp. 1–10.
[23] J. Lan, W. Chen, X. Li, Y. Sun, L. Shu, and F. Deng, "A three-phase multiplexing arm modular multilevel converter with high power density and small volume," *IEEE Trans. Power Electron.*, vol. 37, no. 12, pp. 14587–14600, Dec. 2022.
[24] M. Huang, W. Li, J. Zou, and X. Ma, "Analysis and design of a novel hybrid modular multilevel converter with time-sharing alternative arm converter," *IEEE Trans. Ind. Electron.*, vol. 71, no. 1, pp. 14–26, Jan. 2024.
[25] H. Zhao, W. Chen, G. He, and J. Wang, "A new shared module soft open point for power distribution network," *IEEE Trans. Power Electron.*, vol. 38, no. 3, pp. 3363–3374, Mar. 2023.
[26] J. Zhang et al., "Series–Shunt multiport soft normally open points," *IEEE Trans. Ind. Electron.*, vol. 70, no. 11, pp. 10811–10821, Nov. 2023.
[27] X. Chen, H. Wen, Q. Bu, and W. Liu, "Design of GaN-based voltage reference circuit for a wide-temperature-range operation," in *Proc. Int. Conf. IC Des. Technol.*, 2019, pp. 1–4.
[28] X. Wang, H. Wen, and Y. Zhu, "Review of SiC power devices for electrical power systems: Characteristics, protection, and application," in *Proc. 6th Asia Conf. Power Elect. Eng.*, 2021, pp. 1–5.
[29] A. K. Tripathi, K. Hatua, H. Mirzaee, and S. Bhattacharya, "A three-phase three winding topology for Dual Active Bridge and its D-Q mode control," in *Proc. 27th Annu. IEEE Appl. Power Electron. Conf. Expo.*, 2012, pp. 1368–1372.
[30] R. Chen et al., "Design of 10 kV SiC MOSFET power module based MW-level modular multilevel converter phase-leg," in *Proc. IEEE Appl. Power Electron. Conf. Expo.*, 2024, pp. 1087–1094.
[31] S. Parashar, A. Kumar, N. Kolli, R. K. Kokkonda, and S. Bhattacharya, "Medium voltage bidirectional DC-DC isolator using series connected 10kV SiC MOSFETs," in *Proc. IEEE Appl. Power Electron. Conf. Expo.*, 2020, pp. 3102–3109.
[32] J. Lan, W. Chen, X. He, Y. Xie, and Y. Wang, "The wide multiplexed period three-phase multiplexing arm modular multilevel converter," *IEEE J. Emerg. Sel. Topics Power Electron.*, vol. 11, no. 5, pp. 4929–4944, Oct. 2023.
[33] A. Campos, J. Paez, and P. Dworakowski, "Comparison of modular multilevel converter and neutral point clamped converter topologies for MVDC applications," in *Proc. 25th Eur. Conf. Power Electron. Appl.*, 2023, pp. 1–9.
[34] D. G. Holmes and T. A. Lipo, "Modulation of threephase voltage source inverters," in *Proc. Pulse Width Modulation Power Converters, Princ. Pract.*, 2003, pp. 215–258.
[35] D. G. Holmes and T. A. Lipo, "CarrierBased PWM of multilevel inverters," in *Proc. Pulse Width Modulation Power Converters, Princ. Pract.*, 2003, pp. 453–530.
[36] M. K. Das et al., "10 kV, 120 A SiC half H-bridge power MOSFET modules suitable for high frequency, medium voltage applications," in *Proc. IEEE Energy Convers. Congr. Expo.*, 2011, pp. 2689–2692.

Yutong Chen was born in Jiangsu, China, in 2001. She received the B.S. degree in electrical engineering from Southeast University, Nanjing, China, in 2023. She is currently working toward the M.S. degree in electrical engineering with Southeast University, Nanjing, China.

Her research interests include the control of soft open points and renewable energy generation systems.

Wu Chen (Senior Member, IEEE) was born in Jiangsu, China, in 1981. He received the B.S., M.S., and Ph.D. degrees in electrical engineering from the Nanjing University of Aeronautics and Astronautics, Nanjing, China, in 2003, 2006, and 2009, respectively.

From 2009 to 2010, he was a Senior Research Assistant with the Department of Electronic Engineering, City University of Hong Kong, Hong Kong. In 2010 and 2011, he was a Postdoctoral Researcher with Future Electric Energy Delivery and Management Systems Center, North Carolina State University, Raleigh. Since September 2011, he has been an Associate Research Fellow with the School of Electrical Engineering, Southeast University, Nanjing, China, where he has been a Professor since 2016. His main research interests include soft-switching converters, power delivery, and power electronic system integration.

Dr. Chen is an Associate Editor for IEEE TRANSACTIONS ON INDUSTRIAL ELECTRONICS, *Journal of Power Electronics*, and *CPSS Transactions on Power Electronics and Applications*.

Haixi Zhao received the B.Sc. degree in electrical engineering from Southwest Petroleum University, Chengdu, China, in 2018, and the M.Sc. degree in power electronics and power drives from Hefei University of Technology, Hefei, China, in 2021. He is currently working toward the Ph.D. degree in electrical engineering with the Southeast University, Nanjing, China.

His current research interests include multilevel converter and renewable energy generation systems.

Zewei Hao was born in Inner Mongolia, China, in 1996. He received the B.S. and M.S. degrees in electrical engineering from Wuhan University, Wuhan, China, in 2019 and 2021, respectively. He is currently working toward the Ph.D. degree in electrical engineering with Southeast University, Nanjing, China.

Jianxi Lan (Member, IEEE) was born in Henan, China, in 1992. He received the B.S. degree from Liaoning University of Technology, Liaoning, China, in 2016, the M.S. degree from Tianjin University, Tianjin, China, in 2019, and the Ph.D. degree from Southeast University, Nanjing, China, in 2024, all in electrical engineering.

He is currently a Postdoctoral Researcher with the Southeast University. His research interests include MMC, high power multilevel converter, dc power grid fault isolation, and high power converters for ac–dc hybrid distribution network.

Xuze Wang received the B.Sc. degree in electrical engineering from Southeast University, Nanjing, China, in 2022. He is currently working toward the M.Sc. degree in electrical engineering with the Southeast University, Nanjing, China.

His current research interests include the control and fault traverse of Soft Open Point.

Xin Li was born in Hunan, China, in 2002. He received the B.S. degree in electrical engineering from the Nanjing University of Aeronautics and Astronautics, Nanjing, China, in 2023. He is currently working toward the M.S. degree in electrical engineering with the Southeast University, Nanjing, China.

His current research interests include multilevel converter and renewable energy generation systems.

Runyan Sha was born in Jiangsu, China, in 2000. He received the B.Eng. degree in electrical engineering from Southeast University Chengxian College, Nanjing China, in 2023. He is currently working toward M.Eng. degree in power electronics and power drives with the Southeast University, Nanjing, China.

His current research interest includes flexible interconnection device.

Jiangfeng Wang (Member, IEEE) received the B.S. and Ph.D. degrees in electrical engineering and power electronics and power drives from Nanjing University of Aeronautics and Astronautics, Nanjing, China, in 2012 and 2018, respectively.

From 2019 to 2021, he was a Postdoctoral Research Fellow with Tsinghua University, Beijing, China, and the University of Alberta, Edmonton, AB, Canada. Since March 2022, he has been an Associate Research Fellow with Southeast University, Nanjing, China. His research interests include high-performance power converters, wide bandgap power device application, power quality, and distributed power generation systems.

Dr. Wang is an Associate Editor for the *Journal of Power Electronics* and *Chinese Journal of Electrical Engineering*.

Xin Li (Member, IEEE) received the B.S. and Ph.D. degrees in electrical engineering and automation from Nanjing University of Aeronautics and Astronautics, Nanjing, China, in 2012 and 2018, respectively.

In 2019, he was a Research Engineer with Huawei Technologies Company Ltd., Shanghai, China. From 2020 to 2022, he was a Research Fellow with Nanyang Technological University, Singapore. Since Aug. 2022, has been an Associate Researcher with the School of Electrical Engineering, Southeast University, Nanjing, China. His current research interests include modeling, control and design of PWM converter, resonant converter, and wireless power transfer system.

Wei Jiang (Senior Member, IEEE) was born in China, in 1982. He received the B.S., M.S., and Ph.D. degrees in electrical engineering from Southeast University, Nanjing, China, in 2004, 2008, and 2012, respectively.

He is currently a Professor of electrical engineering with the School of Electrical Engineering, Southeast University. His research interests include the distribution network-mircrogrid coordination and power electronics intergrated power system.

Yubo Yuan (Member, lEEE) was born in China, in 1975. He received the B.Eng. and M.S. degrees from Hohai University, Nanjing, China, in 1997 and 2000, respectively, and the Ph.D. degree from Southeast University, Nanjing, China, in 2004, all in electrical engineering.

From the last 15 years, he has been with the State Grid Jiangsu Electric Power Company Ltd., Electrical Power Research Institute, Nanjing, China, where he is currently a Chief Manager. His research interests include smart distribution power grid control and optimization, control and protection of UHV dc power transmission, control and protection of flexible dc transmission, and smart substation.

Dr. Yuan is currently with the lEEE SA SBLC. He is an Editor of Automation of Electric Power Systems. He is familiar with the work of standardization and is a member of WAMs and Time Synchronization Work Group, Convener of CIGRE B5/D2.67.